Mistuning analysis of a detuned bladed-disk with geometrical nonlinearities

Anthony Picou, Evangéline Capiez-Lernout, Christian Soize, Moustapha Mbaye

GT2019-90820

MISTUNING ANALYSIS OF A DETUNED BLADED-DISK WITH GEOMETRICAL NONLINEARITIES

Anthony Picou*, **Evangéline Capiez-Lernout, Christian Soize**

Laboratoire Modélisation et Simulation Multi Echelle
Université Paris-Est, 5, Bd Descartes, 77454
Marne-La-Valleé Cedex 02, France
Email: anthony.picou@u-pem.fr

Moustapha Mbaye

Safran Tech, Modelling & Simulation
Rue des Jeunes Bois, Châteaufort
Magny-Les-Hameaux, 78772, France
Email: moustapha.mbaye@safrangroup.com

ABSTRACT

This work concerns the nonlinear numerical analysis of mistuned blades for a rotating detuned bladed-disk structure with geometrical nonlinearities. The detuning phenomenon is taken into account through a deterministic approach by modifying material properties of some blades. A nonlinear reduced-order model is obtained by setting up a basis using a double projection method. The mistuning uncertainties are implemented through a nonparametric probabilistic approach for which the level of uncertainties is controlled by a hyperparameter. A numerical application is carried out on a bladed-disk structure made up of 24 blades whose finite element model has about 800,000 dofs exhibiting complex dynamic behaviors.

NOMENCLATURE

b_{NL} Deterministic dynamical amplification factor
$g(t)$ Load in time domain
$\widehat{g}(2\pi\nu)$ Fourier transform of $g(t)$
h Nodal diameter number
j Blade number
j_0 Blade of interest
m Number of eigenvectors
n Number of degrees-of-freedom
s_0 Load intensity
t Time
t_{ini} Initial time
$u^j_\alpha(t)$ Displacement at the tip of blade number j according to local direction $\mathbf{e}_\alpha$
$\widehat{u}^j_\alpha(2\pi\nu)$ Fourier transform of $u^j_\alpha(t)$
$B(2\pi\nu)$ Random dynamical amplification factor
N Dimension of the nonlinear reduced-order model
P Dimension of $[\mathcal{K}^{\mathrm{NL}}]$ matrix

* Corresponding author.

Q Dimension of $[\mathbf{G}_K(\delta_K)]$ random matrix
T Time duration of the excitation
λ_α Eigenvalue number α
δ_K Dispersion parameter
ν Frequency (Hz)
Δt Time sampling
Ω Rotational velocity of the bladed-disk
$\mathbb{B}$ Frequency band of analysis
$\mathbb{B}_e$ Excitation frequency band
$\mathbb{F}$ Spatial distribution vector of the load
$\mathcal{K}^{(2)}_{ijk}$ Quadratic stiffness operator of the reduced-order model
$\mathcal{K}^{(3)}_{ijkl}$ Cubic stiffness operator of the reduced-order model
$\mathcal{P}$ Pattern
$\mathbf{q}_0(t)$ Vector of generalized coordinates related to the first projection basis
$\mathbf{q}(t)$ Vector of generalized coordinates in the time domain
$\mathbf{u}(t)$ Displacement vector in the time domain
$\mathbf{F}(t)$ Load vector
$\mathbf{F}^{\mathrm{NL}}$ Nonlinear internal forces
$\mathcal{F}(t)$ Load vector of the reduced-order-model
φ_α Eigenmode number α
$[C_g(\Omega)]$ Gyroscopic coupling matrix
$[D]$ Damping matrix
$[K_c(\Omega)]$ Centrifugal stiffness matrix
$[K_e]$ Elastic stiffness matrix
$[K_g(\Omega)]$ Geometrical stiffness matrix
$[L_K]$ Part of $[\mathcal{K}^{\mathrm{NL}}]$ matrix decomposition
$[M]$ Mass matrix
$[V]$ Matrix used for constructing the POD basis
$[\mathcal{C}(\Omega)]$ Gyroscopic coupling matrix of the mean reduced-order-model
$[\mathcal{D}]$ Dissipation matrix of the mean reduced-order-model
$[\mathcal{K}]$ Stiffness matrix of the mean reduced-order-model
$[\mathcal{K}^{\mathrm{NL}}]$ Positive matrix containing all the cubic, quadratic and linear elastic stiffness contributions
$[\mathcal{M}]$ Mass matrix of the mean reduced-order-model
$[\mathcal{W}^{(m,N)}]$ Second projection basis of the mean reduced-order-model
$[\Delta\widetilde{\mathcal{K}}]$ Stiffness residual matrix
$[\Phi^m]$ $(n \times m)$ Modal matrix
$[\Psi]$ Global projection matrix
$[\mathbf{G}_K(\delta_K)]$ Random germ matrix given by the nonparametric probabilistic approach
$[\boldsymbol{\mathcal{K}}^{\mathrm{NL}}]$ Random matrix containing all the random cubic, quadratic and linear elastic stiffness contributions

INTRODUCTION

In the framework of linear dynamic analysis of bladed-disk, the intentional detuning has been identified as an efficient technological way for reducing the sensitivity of the forced response of bladed-disks to mistuning induced by small variations of the mechanical properties [1, 2]. Various research concerning the modeling of mistuned bladed-disk have been carried out, with the development of reduced-order models (see for instance [3–6] for linear cases and [7, 8] for nonlinear cases) and of probabilistic approaches [9, 10]. The pattern optimization has been proved to be efficient for reducing the response amplitudes in the linear context. Nevertheless, geometrical nonlinear effects can no longer be neglected with the current technological improvements due to the use of more flexible and lighter materials which sometimes leads to large displacements and strains.

The main objective of this paper is to investigate the effects of geometrical nonlinearities on the nonlinear dynamical behavior of a bladed-disk that is both mistuned and intentionally mistuned. The intentional mistuning is introduced by a given pattern that defines

the spatial distribution of different types of sectors on the full bladed-disk. The mistuning is caused by all the discrepancies that are encountered in the manufacturing process and that break the cyclic symmetry of the structure which may cause dynamical amplification effects. For the sake of clarity "intentional mistuning" and "mistuning" are respectively denoted by "detuning" and "mistuning". We are then interested in quantifying the nonlinear dynamical behavior of the detuned-mistuned bladed-disk assuming the intensity of the load sufficiently high to rightly consider large displacements and large strains.

The main novelty of this work is that both detuning and mistuning phenomena are taken into account within the computational model. The detuning modeling requires to consider two different generating sectors whose finite element meshes are compatible from one sector to another one and to assemble the full structure according to a given pattern. The mistuning phenomena is taken into account through the nonparametric probabilistic approach of uncertainties [9] extended to the geometrical nonlinear context as proposed in [7]. An adapted methodology in accordance with those objectives is implemented. We are therefore interested in the physical nonlinear analysis of such detuned and mistuned bladed-disk structure.

The first Section summarizes the main methodological steps of the nonlinear analysis of such detuned and mistuned bladed-disk structures. Details are given on the choice of the projection basis used to build the nonlinear reduced-order model that is required (1) to optimize the dimension of the nonlinear reduced-order model and (2) to implement the mistuning uncertainties according to the nonparametric probabilistic approach keeping a reasonable size of the random germ matrix. The second Section is devoted to a numerical application for which a simple model representing an industrial detuned and mistuned bladed-disk is considered. In particular, a mistuned case and a mistuned-detuned case are considered. The nonlinear dynamical amplification factors resulting from a uniform excitation over a narrow low-frequency band of excitation are then compared for the two mistuned cases, inside and outside of the frequency band of excitation.

METHODOLOGY

This section is devoted to the construction of a stochastic nonlinear reduced-order model. The constitutive equations of the materials are linear elastic. The external loads are sufficiently large so that the structure undergoes geometrical nonlinear effects induced by the large displacements and strains.

The main difficulty is to obtain a nonlinear stochastic computational model that is able to take into account both detuning and mistuning phenomena considering industrial high-dimensional computational model (HDM). This means that the nonlinear stochastic computational model has to be optimally reduced in order to perform nonlinear stochastic computations with a reasonable computational cost. With the current use of the nonparametric probabilistic strategy, a deterministic nonlinear reduced-order computational model has to be constructed for representing the detuned bladed-disk structure. Uncertainties are then added to this mean nonlinear reduced-order model in order to model the mistuning phenomena. The main steps are as follows:

- A first projection modal basis is computed by solving a generalized eigenvalue problem related to the HDM.
- A second basis is obtained using the Proper-Orthogonal Decomposition (POD) method performed on the structural displacements that are computed with the nonlinear reduced-order model resulting from the projection of the HDM on the first modal basis.
- Mistuning uncertainties are then added to the mean nonlinear reduced-order model obtained from the double projection method.

Nonlinear finite element computational model of a detuned bladed-disk

The detuning is done according to a given pattern, defining the spatial repartition of several different sector types on the full bladed-disk. The finite element meshes of each sector type are compatible from one sector interface to another one. In the rotating frame, the nonlinear differential equation that describes the computational model of the nonlinear dynamical behavior of a rotating detuned bladed-disk as a function of the rotational speed Ω is written as

$$[M]\ddot{\mathbf{u}} + ([D] + [C_g(\Omega)])\,\dot{\mathbf{u}} + ([K_e] + [K_c(\Omega)] + [K_g(\Omega)])\,\mathbf{u} + \mathbf{F}^{\mathrm{NL}}(\mathbf{u}) = \mathbf{F}, \tag{1}$$

in which the $\mathbb{R}^n$-vector $\mathbf{u}$(t) is the vector of unknown displacements. In equation (1), the $(n \times n)$ real matrices $[M]$, $[D]$, $[C_g(\Omega)]$, $[K_e]$, $[K_c(\Omega)]$, $[K_g(\Omega)]$ are respectively the mass matrix with positive definiteness properties, the damping matrix with symmetry and positive definiteness properties, the gyroscopic coupling matrix with skew-symmetry properties, the elastic stiffness matrix with symmetry and positive definiteness properties, the centrifugal stiffness matrix with symmetry and negative definiteness properties, the geometrical stiffness matrix with symmetry and positive definiteness properties. It is assumed that rotational velocity is sufficiently large so that $[K_e] + [K_c(\Omega)] + [K_g(\Omega)]$ is positive definite and there is no static unstability (divergence). In equation (1), the $\mathbb{R}^n$-vector $\mathbf{F}$ results from

the discretization of the external forces and the $\mathbb{R}^n$-vector $\mathbf{F}^{\mathrm{NL}}(\mathbf{q})$ describes the nonlinear internal forces issued from the geometrical nonlinearities.

Numerical construction of an adapted projection basis

A possible approach would consist in solving the generalized eigenvalue problem related to the conservative and linear part of the differential equation (1). Nevertheless, such generalized eigenvalue problem would yield complex eigenvectors because of the skew-symmetry property of the gyroscopic coupling. To avoid this difficulty, the projection basis is built in two steps. First, the previous generalized eigenvalue problem is solved without damping and gyroscopic coupling matrices. Let $\varphi_1, \ldots, \varphi_m$ be the eigenmodes related to the m first eigenvalues, $0 < \lambda_1 \leqslant \lambda_2 \leqslant \cdots \leqslant \lambda_n$ are stored in the $(n \times m)$ real modal matrix $[\Phi^m]$. Such projection modal basis is then used to build the nonlinear reduced-order model related to equation (1). A convergence analysis is carried out with respect to m. Once convergence is reached, the nonlinear reduced-order model is used for computing the forced time-response denoted $\mathbf{q}_0(t)$. The POD basis is obtained by solving the eigenvalue problem for the correlation matrix related to the nonlinear time response $\mathbf{q}_0(t)$. The eigenvectors related to the N most contributing eigenvalues are retained to form the POD vector basis. Let $[\mathcal{W}^{(m,N)}]$ be the $(m \times N)$ real matrix whose columns are these POD vector basis. As explained in [11], this POD vector basis is efficiently generated by computing the N left singular vectors of the real matrix $[V]$ defined by

$$[V]_{ij} = q_{0_i}(t_j)\,\sqrt{\Delta t}\,. \tag{2}$$

The projection basis of the HDM, which allows for constructing the nonlinear reduced-order model, is represented by the $(n \times N)$ real matrix $[\Psi]$ that is written as

$$[\Psi] = [\Phi^m]\,[\mathcal{W}^{(m,N)}]\,. \tag{3}$$

With such reduced-order basis, the nonlinear reduced-order model is written as

$$\mathbf{u}(t) = [\Psi]\,\mathbf{q}(t)\,, \tag{4}$$

$$[\mathcal{M}]\ddot{\mathbf{q}}(t) + (\,[\mathcal{D}] + [\mathcal{C}(\Omega)]\,)\,\dot{\mathbf{q}}(t) + [\mathcal{K}(\Omega)]\mathbf{q}(t) + \boldsymbol{\mathcal{F}}^{\mathrm{NL}}(\mathbf{q}(t)) = \boldsymbol{\mathcal{F}}(t) \quad , \tag{5}$$

in which

$$[\mathcal{M}] = [\Psi]^T[M][\Psi] \tag{6}$$
$$[\mathcal{D}] = [\Psi]^T[D][\Psi] \tag{7}$$
$$[\mathcal{C}(\Omega)] = [\Psi]^T[C_g(\Omega)][\Psi] \tag{8}$$
$$[\mathcal{K}] = [\Psi]^T\,([K_e] + [K_c(\Omega)] + [K_g(\Omega)])\,[\Psi] \tag{9}$$
$$\boldsymbol{\mathcal{F}}(t) = [\Psi]^T\mathbf{F}(t)\,. \tag{10}$$

The reduced quadratic and cubic stiffness operators $\mathcal{K}^{(2)}_{ijk}$, $\{i,j,k\} \in \{1,2,\ldots,N\}^3$ and $\mathcal{K}^{(3)}_{ijk\ell}$, $\{i,j,k,l\} \in \{1,2,\ldots,N\}^4$ are explicitly constructed [12] and the $\mathbb{R}^N$-vector $\boldsymbol{\mathcal{F}}^{\mathrm{NL}}(\mathbf{q})$ is then calculated using

$$\mathcal{F}^{\mathrm{NL}}_i(\mathbf{q}) = \mathcal{K}^{(2)}_{ijk}\,q_j\,q_k + \mathcal{K}^{(3)}_{ijk\ell}\,q_j\,q_k\,q_\ell \quad , \quad \forall \mathbf{q} \in \mathbb{R}^N\,. \tag{11}$$

After solving the nonlinear differential equation (5), for which $\mathbf{q}(t)$ is the $\mathbb{R}^N$-vectors of the unknown generalized coordinates, the physical response is retrieved by using equation (4).

Construction of the stochastic reduced-order model

The stochastic nonlinear computational model corresponds to a probabilistic modeling of the mistuning for the detuned rotating bladed-disk. As previously explained, the nonparametric probabilistic approach of uncertainties is used [9, 13]. Its generalization to the nonlinear geometrical context [14], including a strategy for reducing the size of the germs [15] is used. It involves a positive matrix $[\mathcal{K}^{\rm NL}]$ with order $P = N(N+1)$ containing entries contain all the cubic, quadratic and linear elastic stiffness contributions. The corresponding random matrix $[\boldsymbol{\mathcal{K}}^{\rm NL}]$ is written as:

$$[\boldsymbol{\mathcal{K}}^{\rm NL}] = [L_K][\mathbf{G}_K(\delta_K)][L_K]^T + [\Delta\widetilde{\mathcal{K}}] \tag{12}$$

in which $[L_K]$ is a $(P \times Q)$ real matrix whose columns contain Q, the predominant eigenvectors of matrix $[\mathcal{K}^{\rm NL}]$, where $[\Delta\widetilde{\mathcal{K}}] = [\mathcal{K}^{\rm NL}] - [L_K][L_K]^T$ and where $[\mathbf{G}_K(\delta_K)]$ is the full $(Q \times Q)$ random matrix with $Q \lll P$, constructed using the Maximum Entropy principle [13] and where δ_K is the hyperparameter that allows for controlling the level of uncertainties. By construction the mathematical expectation, $E\{[\boldsymbol{\mathcal{K}}^{\rm NL}]\}$ of random matrix $[\boldsymbol{\mathcal{K}}^{\rm NL}]$ is the deterministic matrix $[\mathcal{K}^{\rm NL}]$. All the details concerning the construction of $[\boldsymbol{\mathcal{K}}^{\rm NL}]$ can be found in [14].

NUMERICAL APPLICATION

The numerical application concerns the nonlinear dynamical analysis of a detuned and mistuned rotating bladed-disk. From an industrial point of view, such an application is of industrial interest when exceptional operating ranges such as severe loads or unstable flutter situations yielding low-damping levels are considered.

Description of the finite element model

The bladed-disk comprises 24 blades and is made of an homogeneous and isotropic elastic material (steel) with Young modulus $2 \times 10^{11} N.m^{-2}$, Poisson's ratio 0.3, and mass density $7650\, Kg.m^{-3}$. In the rotating frame, the disk is clamped at the inner radius of the disk sector. The geometrical characteristics of the generating sector are summarized in Table 1. Software ANSYS has been used to construct the computational model of the reference sector, which is constituted of tridimensional solid finite elements: brick elements with 20 nodes, pyramidal elements with 13 nodes, and tetrahedral elements with 10 nodes. The computational model of the tuned bladed-disk (with 24 blades) has been constructed using the computational model of the sector. The characteristics of the finite element model are given in Table 2. A detuned bladed-disk structure is constructed by defining another sector type (denoted 2), which is obtained

Inner disk Radius	19.8 mm
Outer disk Radius	100 mm
Disk width	20 mm
Blade thickness at root section	4.8 mm
Blade thickness at tip section	2 mm

TABLE 1: Geometrical characteristics of the reference sector

by decreasing the Young modulus of the blade. The Young modulus of the disk remains equal to $2 \times 10^{11} N \times m^{-2}$. Consequently, two patterns are considered: a cyclic one (tuned) denoted as $\mathcal{P}_1$ and a detuned one denoted as $\mathcal{P}_2$. The finite element model of tuned configuration $\mathcal{P}_1$ and the detuned configuration $\mathcal{P}_2$ are shown in Figure 1. The mesh of the finite element sector is shown in Figure 2.

$$\mathcal{P}_1 = [1\,1\,1\,1\,1\,1\,1\,1\,1\,1\,1\,1\,1\,1\,1\,1\,1\,1\,1\,1\,1\,1\,1\,1] \tag{13}$$

$$\mathcal{P}_2 = [1\,1\,1\,1\,1\,2\,2\,2\,2\,2\,1\,1\,1\,1\,1\,2\,2\,2\,2\,2] \tag{14}$$

Structure	Elements	Nodes	DOFs
Blade sector	2,714	6,896	20,688
Disk sector	836	4,554	13,662
Full structure	85,200	265,080	787,176

TABLE 2: Characteristics of the finite element model

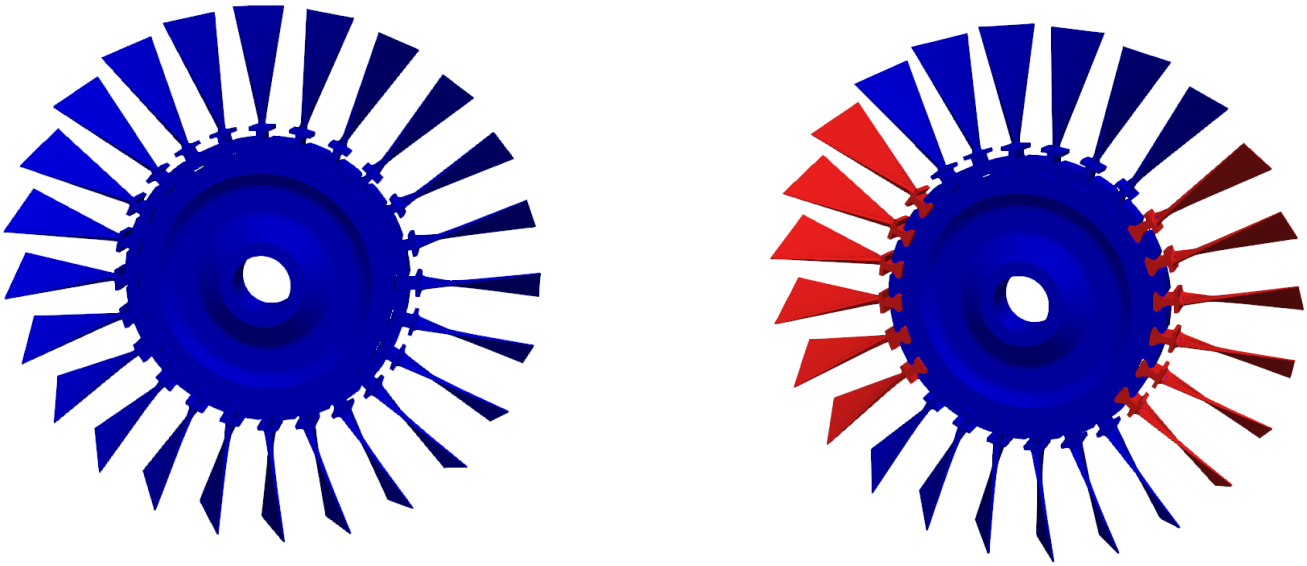

FIGURE 1: Configurations $\mathcal{P}_1$ (left) and $\mathcal{P}_2$ (right)

Eigenfrequencies of the linearized tuned rotating bladed-disk

Figure 3 displays the Campbell diagram representing the evolution of the eigenfrequencies according to the rotational velocity Ω for the tuned case (pattern $\mathcal{P}_1$). Figure 4 displays the graph of eigenfrequencies $\nu_\alpha = \sqrt{\lambda_\alpha}$ as a function of the nodal diameter number h for the linearized tuned rotating bladed-disk (configuration $\mathcal{P}_1$) for which the rotational speed is $\Omega = 465\, rad.s^{-1}$.

Defining the external load

An $h = 20$ engine order excitation is chosen for which there are two close eigenfrequencies from two different classes of eigenmodes. In the time domain, the load vector $\mathbf{F}(t)$ is defined by,

$$\mathbf{F}(t) = s_0\, g(t)\, \mathbb{F} \quad . \tag{15}$$

The time-function $g(t)$ is defined for $t \in \mathbb{R}$ and is constructed so that its Fourier transform is $|\widehat{g}(2\pi\nu)| = 1$ on the frequency band $\mathbb{B}_e = [1000, 1600]\, Hz$ of excitation and zero outside $\mathbb{B}_e$. In the numerical process, the signal $g(t)$ is truncated by choosing $t_{ini} = -0.065\, s$ such that $g(t_{ini}) = 0$ with a time duration $T = 0.35\, s$, ensuring the low frequencies located outside $\mathbb{B}_e$ to be captured when considering nonlinear dynamical responses. Figures 5 and 6 show the graph $t \to g(t)$ and its Fourier transform $\nu \to |\widehat{g}(2\pi\nu)|$. The spatial distribution of the external load is a normalized vector $\mathbb{F}$ for which all directions related to the node located at the tip of each blade are simultaneously excited and the load intensity is given by $s_0 = 1\, N$. The dynamical analysis is performed in the time domain. Then a Fourier Transform of the time responses allows for analyzing the nonlinear dynamical responses in the frequency domain.

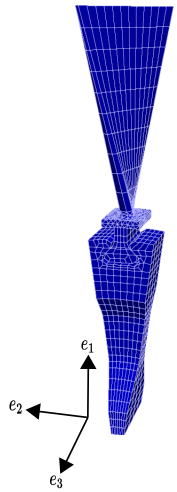

FIGURE 2: Mesh of the finite element sector

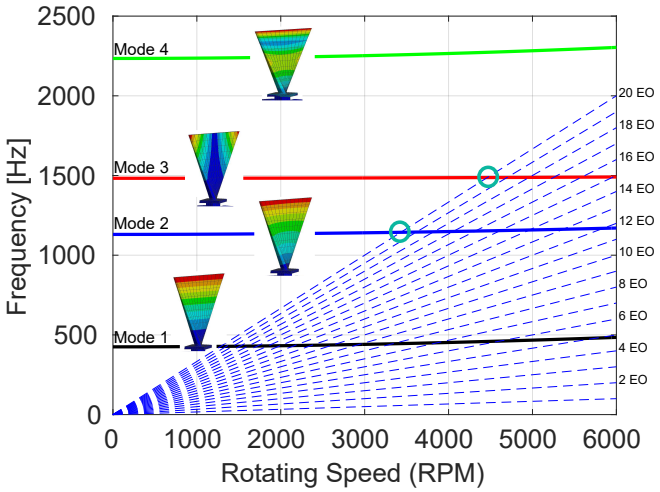

FIGURE 3: Graph of $\Omega \mapsto \nu_\alpha(\Omega)$ defining the Campbell diagram of the tuned structure (pattern $\mathcal{P}_1$).

NUMERICAL PARAMETER CONCERNING THE STOCHASTIC REDUCED-ORDER MODEL

We are interested in analyzing the nonlinear dynamical response in the frequency band of analysis $\mathbb{B} = [0, 4\,000]\,Hz$. For each pattern, the first generalized eigenvalue problem is solved and a convergence analysis of the nonlinear dynamical responses showed that $m = 145$ eigenmodes were required for the first reduced-order basis. The convergence analysis with respect to the responses computed with the first nonlinear reduced-order model shows that $N = 55$ vectors in the second reduced-order basis (constructed by the POD method) are sufficient to reproduce the nonlinear dynamical behavior in frequency band $\mathbb{B}$ [16]. In the following, all calculations are carried out with a reduced-order basis characterized by $(m,N) = (145,55)$. Concerning the size of the random germ, a convergence analysis has shown that a good approximation was obtained for $Q = 500 \ll N(N+1) = 3\,080$.

Nonlinear dynamical analyses of both tuned and detuned rotating bladed-disk

In this Section, the nonlinear deterministic dynamical response of the tuned and detuned bladed-disk is considered. In the following, the subscripts NL and LIN are used for the nonlinear case and for the linear case (when a quantity is used either for NL or for LIN, the

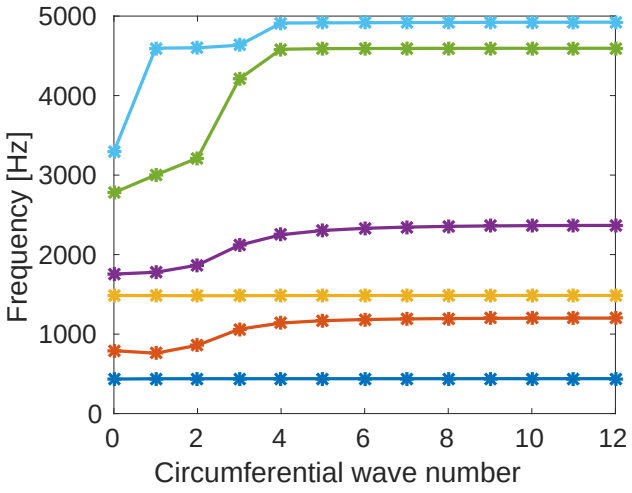

FIGURE 4: Graph $h \mapsto \nu_\alpha(h)$ of the eigenfrequencies ν_α related to the tuned pattern $\mathcal{P}_1$ of the rotating bladed-disk as a function of the nodal diameter number h.

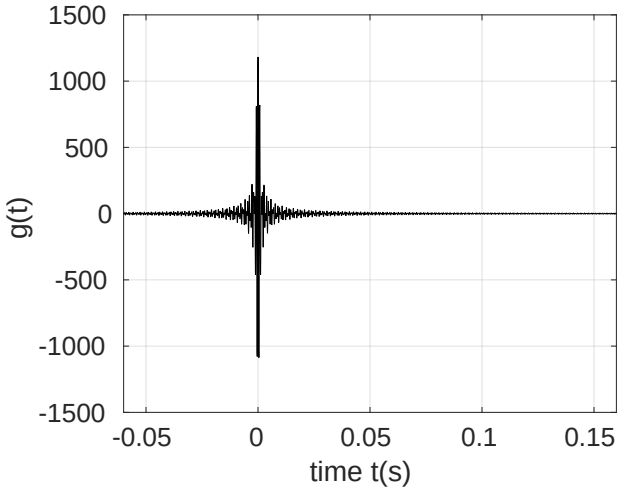

FIGURE 5: Graph of $t \mapsto g(t)$.

subscript is removed). Let $u_\alpha^j(t)$ be the time displacement of blade j according to local direction $\mathbf{e}_\alpha$. For a given pattern, the observation $|||\mathbf{u}^j|||$ is defined by

$$|||\mathbf{u}^j|||^2 = \max_t ||\mathbf{u}^j(t)||^2 \quad \text{with} \quad ||\mathbf{u}^j(t)||^2 = \sum_{\alpha=1}^{3} |u_\alpha^j(t)|^2 . \tag{16}$$

For each pattern, the response related to the most responding blade j_0 in the time domain is considered. We then have

$$j_0 = \arg \left\{ \max_j |||\mathbf{u}^j||| \right\} \quad . \tag{17}$$

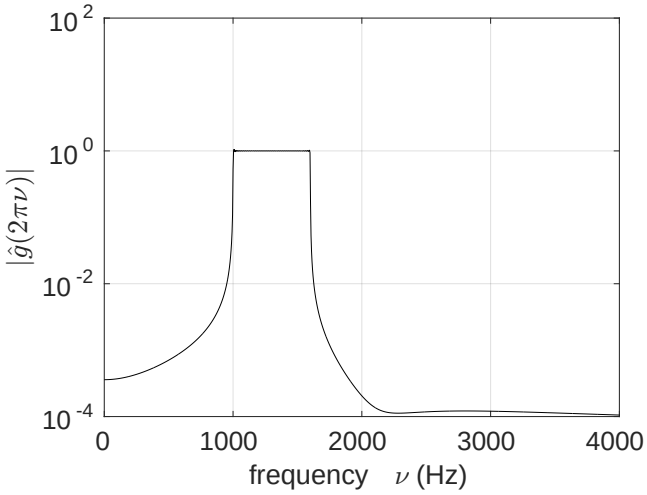

FIGURE 6: Graph of $\nu \mapsto |\widehat{g}(2\pi\nu)|$.

Figures 7 and 8 display the graphs of $t \mapsto u^{j_0}_{2,\mathrm{LIN}}(t)$ for both patterns $\mathcal{P}_1$ and $\mathcal{P}_2$. It can be seen that both tuned and detuned structures yield different responses in the time domain. Figures 9 and 10 respectively display the graphs of $t \mapsto u^{j_0}_{2,\mathrm{NL}}(t)$ for pattern $(\mathcal{P}_1)$ and pattern $(\mathcal{P}_2)$. Table 3 summarizes the maximum displacements for both linear and nonlinear cases corresponding to pattern $\mathcal{P}_1$ and $\mathcal{P}_2$

	Linear	Nonlinear
$\mathcal{P}_1$	$1.48 \times 10^{-3}\, m$	$5.33 \times 10^{-4}\, m$
$\mathcal{P}_2$	$1.67 \times 10^{-3}\, m$	$6.18 \times 10^{-4}\, m$

TABLE 3: Maximum displacements in the time domain

and related to a load intensity $s_0 = 1N$. It is clearly seen that this load yields to significant geometrical effects that stiffen the nonlinear dynamical response of the tuned and detuned structures. The observed nonlinear time responses look more irregular, suggesting numerous resonances contributions outside $\mathbb{B}_e$. The nonlinear dynamical response is then analyzed in the frequency domain. Let $\widehat{u}^{j_0}_{\alpha}(2\pi\nu)$ be the Fourier Transform of $u^{j_0}_{\alpha}(t)$. Figure 11 displays the graph of $\nu \mapsto ||\widehat{\mathbf{u}}^{j_0}_{\mathrm{LIN}}(2\pi\nu)||$ (red line) and the graph of $\nu \mapsto ||\widehat{\mathbf{u}}^{j_0}_{\mathrm{NL}}(2\pi\nu)||$ (blue line) related to pattern $\mathcal{P}_1$. Figure 12 displays the graph of $\nu \mapsto ||\widehat{\mathbf{u}}^{j_0}_{\mathrm{LIN}}(2\pi\nu)||$ (red line) and the graph of $\nu \mapsto ||\widehat{\mathbf{u}}^{j_0}_{\mathrm{NL}}(2\pi\nu)||$ (blue line) corresponding to pattern $\mathcal{P}_2$. For both patterns, secondary resonances induced by the geometrical nonlinear effects appear below and above excitation frequency band $\mathbb{B}_e$. It should be underlined that the major effects of the geometrical nonlinearities is to induce an indirect excitation outside the frequency excitation frequency band as shown in [7, 16] in turbomachinery context or in [17] in fluide-structure interaction.

Nonlinear dynamical analysis of the mistuned-detuned rotating bladed-disk

Unlike the previous Section where the observations related to the deterministic case were denoted by lowercase letters, the random observations corresponding to the stochastic case (presence of mistuning) are similarly denoted by capital letters. In this part, we are interested in the nonlinear dynamical stochastic analysis of the mistuned-detuned rotating bladed-disk. Let $B_{\mathrm{NL}}(2\pi\nu)$ be the random

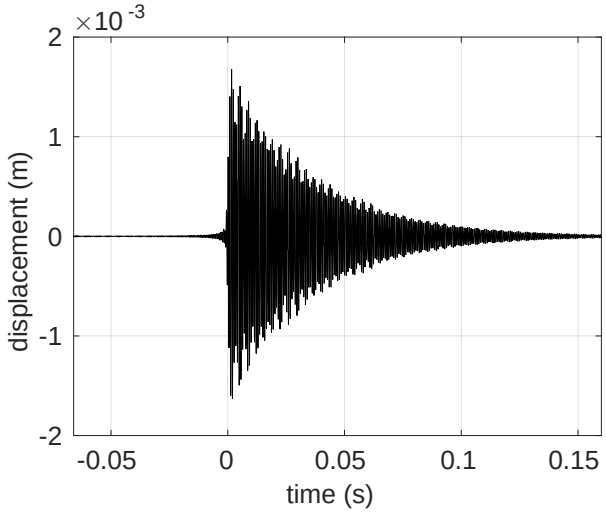

FIGURE 7: Linear dynamical analysis in the time domain: graph of $t \mapsto u_{2,\mathrm{LIN}}^{j_0}(t)$ corresponding to pattern $\mathcal{P}_1$.

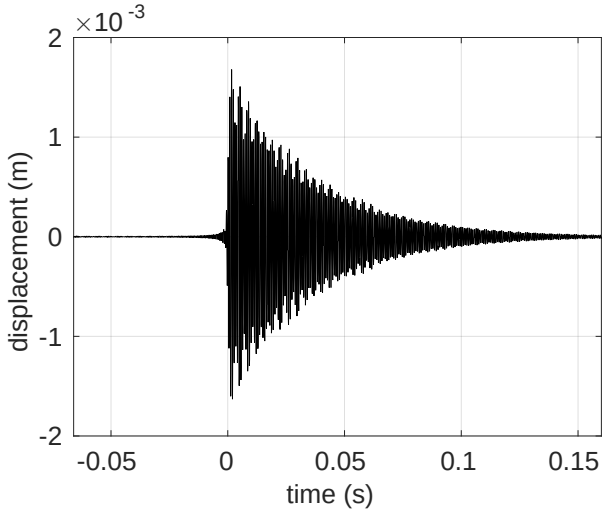

FIGURE 8: Linear dynamical analysis in the time domain: graph of $t \mapsto u_{2,\mathrm{LIN}}^{j_0}(t)$ corresponding to pattern $\mathcal{P}_2$.

amplification dynamic factor defined by,

$$B_{\mathrm{NL}}(2\pi\nu) = \frac{||\widehat{\mathbf{U}}_{\mathrm{NL}}^{j_0}(2\pi\nu)||}{|||\widehat{\mathbf{u}}_{\mathrm{NL}}^{j_0,tuned}|||} \quad , \tag{18}$$

in which $|||\widehat{\mathbf{u}}_{\mathrm{NL}}^{j_0,tuned}||| = \max_{\nu\in\mathbb{B}_e} ||\widehat{\mathbf{u}}_{\mathrm{NL}}^{j_0,tuned}(2\pi\nu)||$. Figures 13 to 14 display the deterministic dynamical amplification factor $\nu \mapsto b_{\mathrm{NL}}(2\pi\nu)$ (thick dashed line). The corresponding confidence region of random observation $B_{\mathrm{NL}}(2\pi\nu)$ for $\delta = 0.1$ and $\delta = 0.3$ corresponding to a probability level of 0.95. In these figures, the excitation frequency band $\mathbb{B}_e$ is represented by the light blue area. It can be seen that the nonlinear dynamical behavior is very sensitive to uncertainties outside the excitation frequency band. These results are obtained for a given pattern of the detuned structure.

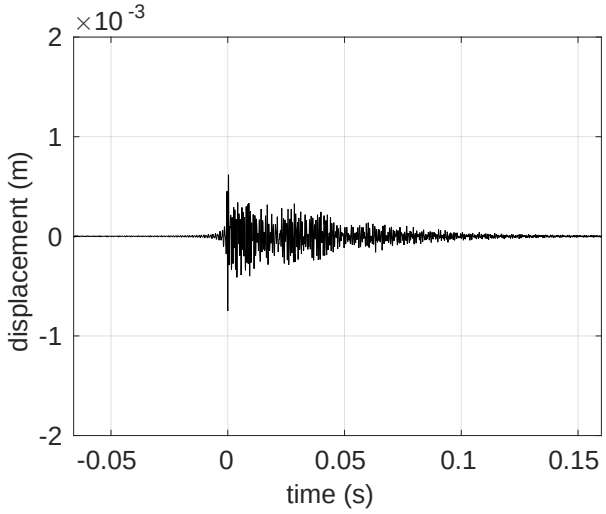

FIGURE 9: Nonlinear dynamical analysis in the time domain: graph of $t \mapsto u_{2,\mathrm{NL}}^{j_0}(t)$ corresponding to pattern $\mathcal{P}_1$.

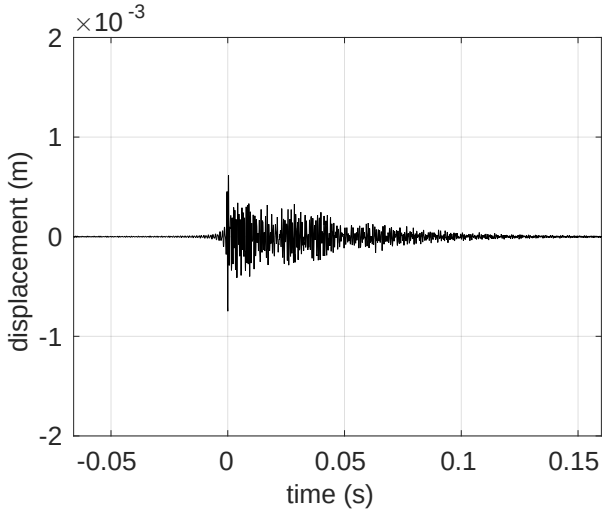

FIGURE 10: Nonlinear dynamical analysis in the time domain: graph of $t \mapsto u_{2,\mathrm{NL}}^{j_0}(t)$ corresponding to pattern $\mathcal{P}_2$.

CONCLUSION

A methodology adapted to the modeling of the mistuned and the detuned rotating bladed-disk has been detailed and applied to a simple model representing an industrial bladed-disk. The results highlight the indirect excitation of the structure through the geometrical nonlinearities, above and below the excitation frequency band. Furthermore, the dynamical analysis of the considered detuned and mistuned rotating bladed-disk has allowed the sensitivity of the structure outside the excitation frequency band to be quantified. The computational implementation of the proposed methodology shows that we are able to propose a nonlinear geometrical analysis of a detuned-mistuned rotating bladed-disk structure. In the present case, the considered detuned pattern is not optimized regarding the dynamical amplification factor. An interesting perspective is to perform an optimization of the detuning with respect to dynamical criteria involving the amplification factor that occur in the excitation frequency band as well as the local amplification factors that occurs outside the excitation frequency band.

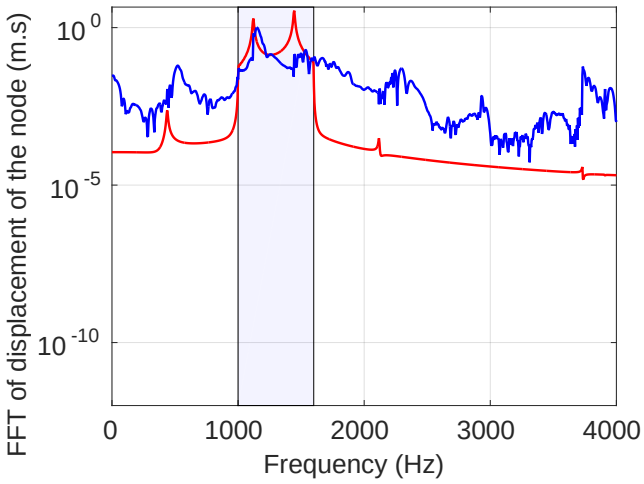

FIGURE 11: Nonlinear dynamical analysis of the deterministic tuned structure (pattern $\mathcal{P}_1$: graphs of $\nu \mapsto ||\widehat{\mathbf{u}}^{j_0}_{\mathrm{LIN}}(2\pi\nu)||$ (red line) and $\nu \mapsto ||\widehat{\mathbf{u}}^{j_0}_{\mathrm{NL}}(2\pi\nu)||$ (blue line) and excitation frequency band $\mathbb{B}_e$ (light blue area).

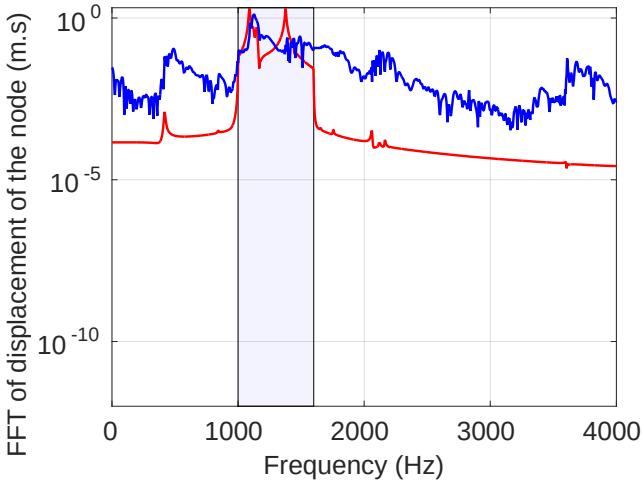

FIGURE 12: Nonlinear dynamical analysis of the deterministic detuned structure (pattern $\mathcal{P}_2$: graphs of $\nu \mapsto ||\widehat{\mathbf{u}}^{j_0}_{\mathrm{LIN}}(2\pi\nu)||$ (red line) and $\nu \mapsto ||\widehat{\mathbf{u}}^{j_0}_{\mathrm{NL}}(2\pi\nu)||$ (blue line) and excitation frequency band $\mathbb{B}_e$ (light blue area).

ACKNOWLEDGMENT

SafranTech is gratefully acknowledged for the permission to publish this work.

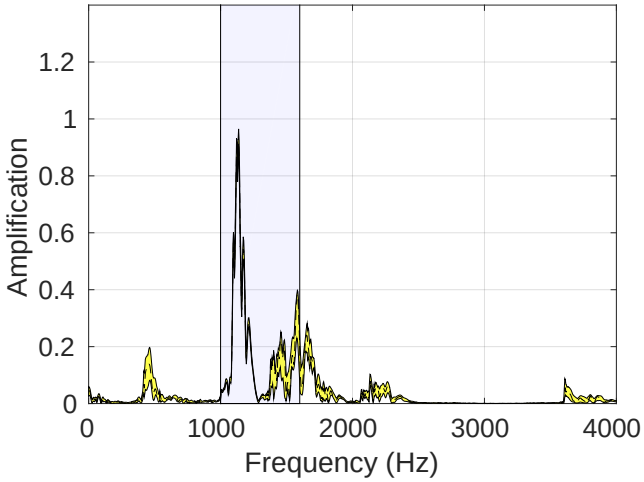

FIGURE 13: Nonlinear mistuning analysis of the detuned structure (pattern $\mathcal{P}_2$): graph of $\nu \mapsto b_{\mathrm{NL}}(2\pi\nu)$ (thick dashed line), confidence region of $B_{\mathrm{NL}}(2\pi\nu)$ (yellow area) and excitation frequency band $\mathbb{B}_e$ (light blue area) for $\delta = 0.1$.

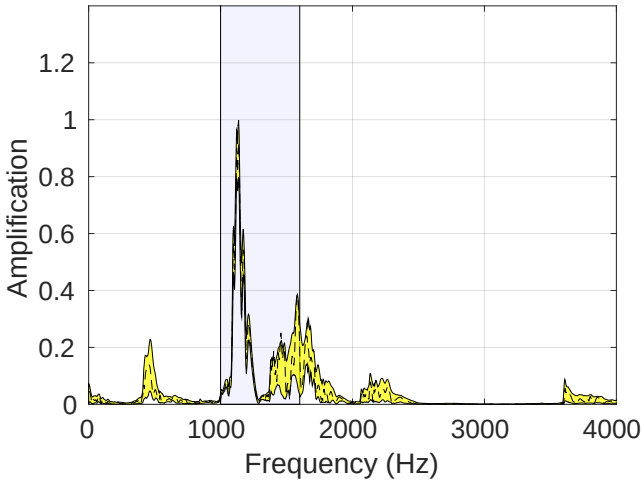

FIGURE 14: Nonlinear mistuning analysis of the detuned structure (pattern $\mathcal{P}_2$): graph of $\nu \mapsto b_{\mathrm{NL}}(2\pi\nu)$ (thick dashed line), confidence region of $B_{\mathrm{NL}}(2\pi\nu)$ (yellow area) and excitation frequency band $\mathbb{B}_e$ (light blue area) for $\delta = 0.3$.

REFERENCES

[1] D.J. Ewins. The effects of detuning upon the forced vibrations of bladed disks. *Journal of Sound and Vibration*, 9(1):65–79, 1969.

[2] D.S. Whitehead. The maximum factor by which forced vibration of blades can increase due to mistuning. *ASME Journal of Engineering for Gas Turbines and Power*, 120(1):115–119, 1998.

[3] M.P. Castanier, G. Ottarson, and C. Pierre. Reduced order modeling technique for mistuned bladed disks. *Journal of Vibration and Acoustics*, 119(3):439–447, 1997.

[4] M-T. Yang and J.H. Griffin. A reduced-order model of mistuning using a subset of nominal system modes. *ASME Journal of Engineering for Gas Turbines and Power*, 123(3):893–900, 2001.

[5] R. Bladh and M.P. Castanier. Component-mode-based reduced order modeling techniques for mistuned bladed disks-part 1: The-

oretical models. *Journal of Engineering for Gas Turbines and Power*, 123(1):89–99, 2001.
[6] Alok Sinha. Reduced-order model of a bladed rotor with geometric mistuning. *Journal of Turbomachinery*, 131(3):031007, 2009.
[7] E. Capiez-Lernout, C. Soize, and M. Mbaye. Mistuning analysis and uncertainty quantification of an industrial bladed disk with geometrical nonlinearity. *Journal of Sound and Vibration*, 356:124–143, 2015.
[8] Aurelien Grolet and Fabrice Thouverez. Computing multiple periodic solutions of nonlinear vibration problems using the harmonic balance method and groebner bases. *Mechanical Systems and Signal Processing*, 52:529–547, 2015.
[9] C. Soize. A nonparametric model of random uncertainties for reduced matrix models in structural dynamics. *Probabilistic Engineering Mechanics*, 15(3):277–294, 2000.
[10] MP Mignolet and C Soize. Nonparametric stochastic modeling of linear systems with prescribed variance of several natural frequencies. *Probabilistic Engineering Mechanics*, 23(2-3):267–278, 2008.
[11] Evangéline Capiez-Lernout, Christian Soize, and M-P Mignolet. Post-buckling nonlinear static and dynamical analyses of uncertain cylindrical shells and experimental validation. *Computer Methods in Applied Mechanics and Engineering*, 271:210–230, 2014.
[12] E. Capiez-Lernout, C. Soize, and M.-P. Mignolet. Computational stochastic statics of an uncertain curved structure with geometrical nonlinearity in three-dimensional elasticity. *Computational Mechanics*, 49(1):87–97, 2012.
[13] C Soize. *Uncertainty Quantification: An Accelerated Course with Advanced Applications in Computational Engineering*. Springer, 2017.
[14] M.-P. Mignolet and C. Soize. Stochastic reduced order models for uncertain geometrically nonlinear dynamical systems. *Computer Methods in Applied Mechanics and Engineering*, 197(45-48):3951–3963, 2008.
[15] E. Capiez-Lernout and C. Soize. An improvement of the uncertainty quantification in computational structural dynamics with nonlinear geometrical effects. *International Journal for Uncertainty Quantification*, 7(1), 2017.
[16] A. Picou, E. Capiez-Lernout, C. Soize, and M. Mbaye. Effects of geometrical nonlinearities for a rotating intentionally mistuned bladed-disk. In *Conference on Noise and Vibration Engineering (ISMA 2018)*, pages 1–11. KU Leuven, 2018.
[17] Quentin Akkaoui, Evangéline Capiez-Lernout, Christian Soize, and Roger Ohayon. Nonlinear dynamical analysis of a fluid-structure computational model with sloshing and capillarity. In *Conference on Noise and Vibration Engineering (ISMA 2018)*, pages 1–12. KU Leuven, 2018.